Hindawi
Geofluids
Volume 2022, Article ID 4030000, 17 pages
https://doi.org/10.1155/2022/4030000

WILEY | Hindawi

Research Article

Experimental Study on the Influence of Hydromechanical Boundary Conditions on Shear-Flow Coupling Characteristics of Granite Joints

Yangbing Cao,[1,2] Yang Wu,[1] Xiangxiang Zhang,[1] Zhi Liu,[1] Weiguo Gong,[1] and Zhenping Huang[1]

[1]*Zijin School of Geology and Mining, Fuzhou University, Fuzhou 350108, China*
[2]*Key Laboratory of Geohazard Prevention of Hilly Mountains, Ministry of Natural Resources (Fujian Key Laboratory of Geohazard Prevention), Fuzhou 350003, China*

Correspondence should be addressed to Zhi Liu; lzhi0518@163.com

Received 6 June 2022; Accepted 1 August 2022; Published 22 August 2022

Academic Editor: Su Shan-Jie

The instability of jointed rock mass is usually the shear process of the rock mass along discontinuities under the influence of groundwater flow. By conducting laboratory tests and numerical experiments on the shear-flow coupling of rock joints under constant normal stiffness (CNS) and constant normal stress (CNL) boundary conditions, the influence of normal boundary conditions and seepage pressure on the shear mechanical and flow characteristics of joints were investigated. The test results were as follows: The joint shear stiffness, peak, and residual shear strength under the CNS boundary condition were predominantly larger than those under the CNL boundary condition. Overall, these parameters were positively correlated with the initial normal stress σ_{n0}. When $\sigma_{n0} > 2$ MPa, the postpeak shear stress of the CNS boundary condition showed a sharp decrease, whereas that of the CNL boundary condition changed from a slowly decreasing type ($\sigma_{n0} = 4$ MPa, 6 MPa) to a sharply decreasing type at $\sigma_{n0} = 8$ MPa. The peak dilation rate under the CNS boundary condition at all levels of normal stress was lower than that of CNL, and the strain softening in postpeak of the latter was more remarkable. In the process of joint shear, the hydraulic aperture displayed a four-stage variation law of "steady-sudden increase-slow increase-basically stable." Moreover, the hydraulic aperture under the CNS boundary condition was always lower than that under the CNL boundary condition. The seepage pressure increased from 0.5 MPa to 1.5 MPa, and the average hydraulic aperture in the stable stage under normal stress at all levels increased from 0.146 mm to 0.187 mm. In addition, the average peak shear stress and average shear stiffness decreased by 0.9 MPa and 0.83 GPa/m, respectively. We also established a numerical model of a real rough three-dimensional joint, compiled a calculation program for the shear-flow process of a joint under CNS boundary conditions, and visualized the flow channel inside the joint. The seepage flow bypassed the area where the joints contacted each other, forming obvious flow channels. The flow rate increased at the intersection of the flow channels.

1. Introduction

The instability of rock slopes and caverns surrounding rocks is typically triggered by rainfall or groundwater seepage, which is essentially a shear-flow coupling process of loaded rock along the discontinuity under the action of water flow. Therefore, for most jointed rock instability problems, this can be attributed to the effect of hydromechanical boundary conditions on the coupling shear-flow characteristics of the joints. Current researches are focused on the response of the deformation and flow characteristics of joints to normal stress σ_n and seepage pressure P. They predominantly concentrate on the variation law of hydraulic conductivity and flow rate of joints during the shearing process of joints under constant normal stress (CNL) boundary conditions, as well as the refinement and modification of the cubic law [1–5]. Shen et al. [6] established the relationship between normal stress and joint contact area based on laboratory test data

Table 1: Joint shear-flow coupling test protocol.

Test groups	Normal stiffness (GPa·m^{-1})	Initial normal stress (MPa)	Seepage pressure (MPa)
I	0	2, 4, 6, 8	1
	1.8	2, 4, 6, 8	1
II	1.8	2, 4, 6, 8	0.5, 1, 1.5

Figure 1: Granite joint using splitting method.

Table 2: Physical and mechanical parameters of the granite and UHPC.

Material type	ρ (kg·m^3)	σ_c (MPa)	σ_t (MPa)	φ_b ($^\circ$)	E (GPa)	υ
Granite	2.63×10^3	146.3	7.0	27.1	17.6	0.18
UHPC	2.32×10^3	145.6	9.1	30.4	14.7	0.21

Figure 2: Rock joint shear-flow coupling test system.

and showed that flow rate decreased with increasing contact area. The results of Ahola et al. [7] demonstrated that an increase in normal stress leads to a decrease in hydraulic conductivity. Lee and Cho [8] and Esaki et al. [9] observed that the hydraulic conductivity of joint decreases with increasing normal load and increases with increasing shear displacement, whereas Fang et al. [10] concluded that the hydraulic conductivity of the joint gradually decreases with shear displacement under high normal stress. Yang et al. [11] observed that joint hydraulic conductivity is more sensitive to shear stress than normal stress. Xiong et al. [12] conducted laboratory and numerical shear-flow coupling tests to establish the relationship between hydraulic conductivity and mechanical aperture. Zhou et al. [13] considered the dilation effect caused by normal stress and shear stress and derived a theoretical analytical equation for fracture permeability in the shear process. Shen et al. [14] concluded that the fracture transmissivity increases continuously with

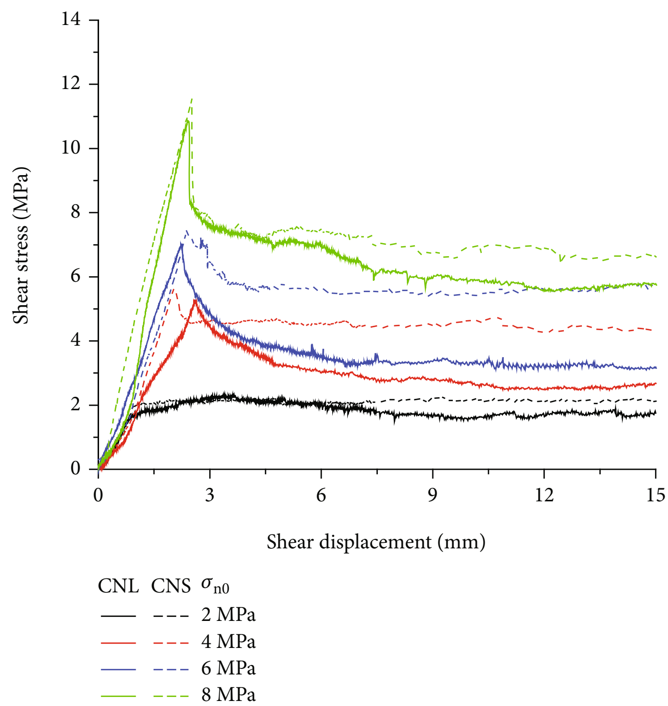

Figure 3: Curves of shear stress with shear displacement.

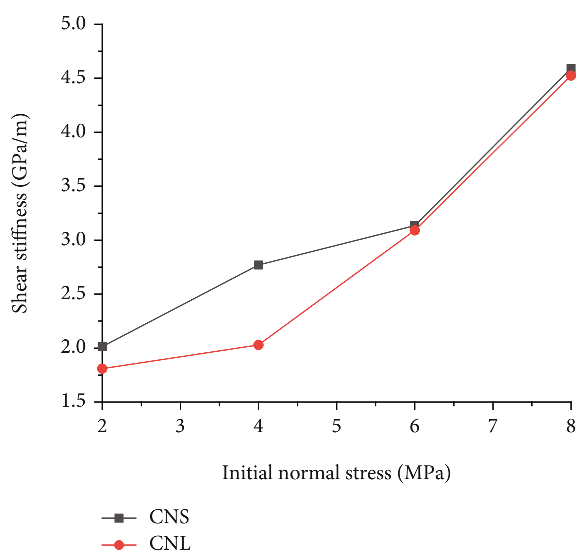

Figure 4: Curves of shear stiffness with initial normal stress.

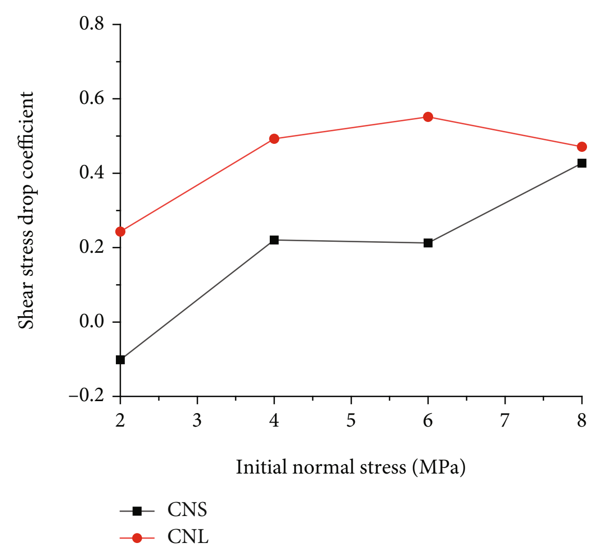

Figure 5: Curves of shear stress drop coefficient with initial normal stress.

shear displacement before the peak shear strength and is essentially constant after the peak shear strength when the effective normal stress is greater than 10 MPa.

With advancements in research, researchers have conducted numerous studies on the shear mechanics and deformation characteristics of joints under constant normal stiffness (CNS) boundary conditions [15–18]. Cui et al. [19] demonstrated that the shear strength, peak normal stress, and peak normal displacement of joints under CNL boundary conditions were significantly lower than those under CNS, which is consistent with the experimental results derived by Indraratna et al. [20, 21]. Direct shear tests under both CNS and CNL normal boundary conditions have also been carried out [22–24], and the results demonstrated that CNS boundary conditions increased the shear strength of the joints. In addition, the peak and residual shear stress increased significantly with an increase in the initial normal stress. With regard to the shear-flow coupling characteristics of joints under CNS boundary conditions, Olsson and Barton [25] indicated that hydraulic conductivity decreases with increasing normal stiffness, but the highest seepage pressure imposed by the test can only reach 0.04 MPa. Chiba et al. [26] also studied the variation law of hydraulic characteristics. However, the shear

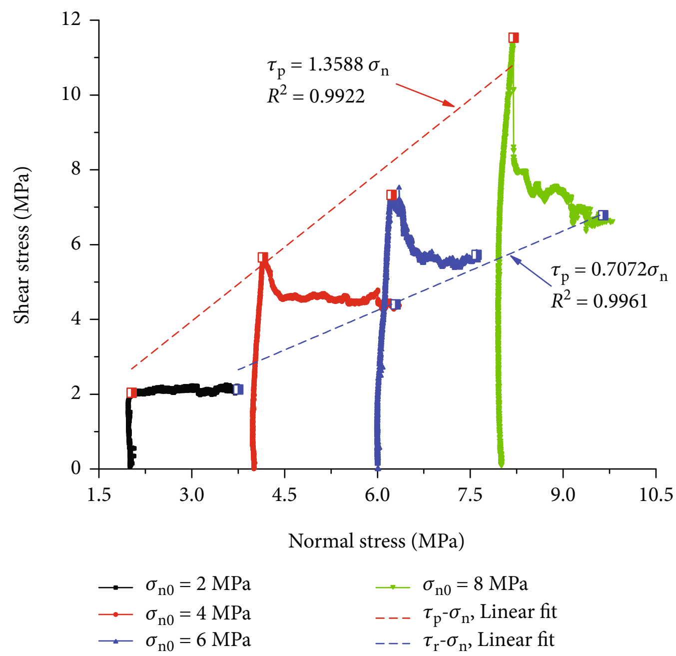

Figure 6: Path evolution curves of shear stress with normal stress (CNS).

displacement of this test system could only reach 3 mm, which does not reflect the flow behavior of the entire joint shear process. Li et al. [27] carried out the shear-flow coupling test under CNS and CNL conditions and studied the variation law of the flow rate of the joint with the contact area during the shear process. Most studies on the effect of seepage pressure on the shear-flow coupling characteristics of joints have focused on the effect of seepage pressure on the seepage characteristics and normal deformation characteristics of joints [28–31].

Cao et al. [32] conducted a shear-flow coupling test on sawtooth joints to study the variation in the flow rate and hydraulic aperture with seepage pressure. Rong et al. [33] displayed that the hydraulic gradient increases with an increase in the flow rate. Di et al. [34] concluded that hydraulic conductivity is positively correlated with seepage pressure and the particle size of the joint material. Zhang et al. [35] demonstrated that the greater the seepage pressure, the greater the flow velocity, and proposed an improved relationship between the flow rate and hydraulic aperture. Some scholars have reported that the normal deformation of the joint increased with an increase in seepage pressure [36, 37]. However, Xia et al. [38] concluded that the normal deformation of the joint decreases with an increase in seepage pressure under CNS boundary conditions.

In summary, existing studies on the coupled shear-flow characteristics of joints have mostly discussed the flow characteristics of joints under CNS or CNL conditions and have predominantly focused on the effects of normal load and seepage pressure on flow rate, hydraulic conductivity, and other seepage characteristics. Unfortunately, less attention has been paid to the variation of mechanical characteristics such as shear stiffness, shear stress, and hydraulic aperture of joints under the action of seepage pressure and different normal boundary conditions. Moreover, the law of the influence of seepage pressure on the dilation effect of joints under CNS boundary conditions is still controversial. Based on these deficiencies, laboratory tests on the coupled shear-flow of granite joints were carried out with normal stiffness K_n, initial normal stress σ_{n0}, and seepage pressure P as variables. It was combined with numerical experiments to reveal the influence law of hydromechanic boundary conditions on the mechanical characteristics of joints, such as shear stiffness, shear stress, and hydraulic aperture.

2. Experimental Protocol and Methods

2.1. Test Protocol. The background of this study is based on water-sealed storage caverns; relevant parameters of granite are set according to the engineering geological and hydrogeological conditions of the water-sealed storage caverns. In this study, normal stiffness, initial normal stress, and seepage pressure were utilized as variables to investigate the effects of hydromechanic boundary conditions on the coupled shear-flow characteristics of granite joints. The initial normal stress is determined according to the circumferential stress and joint production of the cavern chamber of a water-sealed storage cavern, and the seepage water pressure is determined according to the groundwater environment in which the cavern storage is located [39]. K_n is equivalent to the elastic foundation coefficient of the granite rock at the small deformation stage, which was calculated as 1.8 GPa/m according to the literature [40]. The seepage pressure was set to 1 MPa, and the initial normal stresses were applied to 2 MPa, 4 MPa, 6 MPa, and 8 MPa, respectively. Subsequently, the shear-flow coupling tests of granite joints under CNS and CNL conditions were carried out, corresponding to test group I in Table 1. Group I was designed

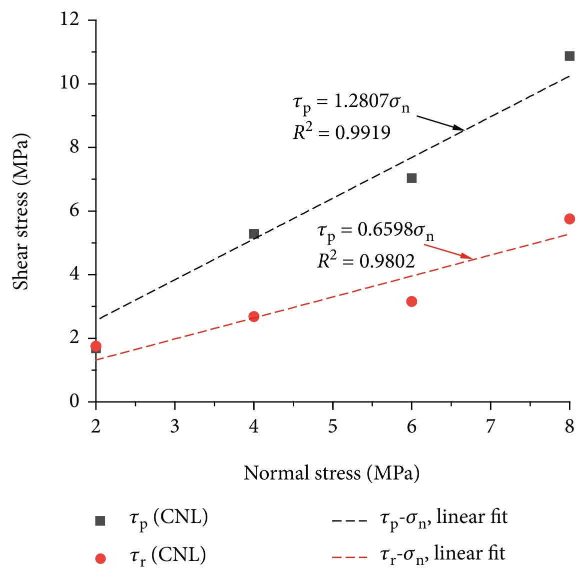

Figure 7: Variation of peak and residual shear stress with normal stress (CNL).

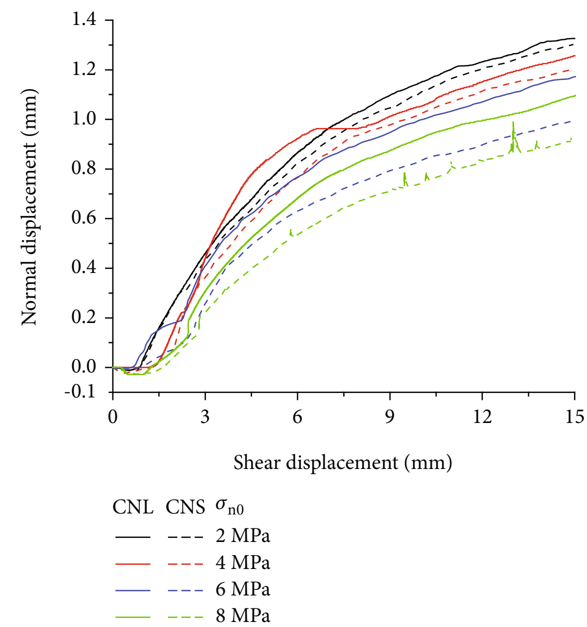

Figure 8: Curves of normal displacement with shear displacement.

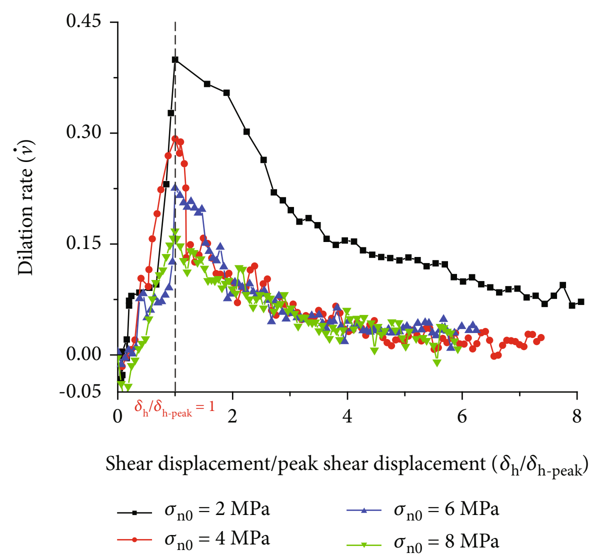

Figure 9: Curves of the dilation rate with λ (CNS).

to investigate the influence of normal boundary conditions on the shear-flow coupling characteristics of granite joints. To explore the response of hydromechanical characteristics to seepage pressure, three levels of seepage pressure (0.5 MPa, 1.0 MPa, and 1.5 MPa) were set. For each level of seepage pressure, joint shear-flow coupling tests (CNS boundary condition) were conducted under normal stresses of 2 MPa, 4 MPa, 6 MPa, and 8 MPa, as shown in test group II in Table 1.

2.2. Specimen Preparation. The effect of normal boundary conditions on the coupled shear-flow characteristics of joints was investigated based on real rough three-dimensional granite joints. The joint samples were made by cutting and grinding in situ granite and then splitting it (Figure 1).

A noncontact 3D scanner was used to scan the surface morphology of the joints, and the point cloud data of the joint surfaces were accurately obtained and processed. The joint roughness coefficient JRC was used to evaluate the joint roughness, which was calculated using Equations (1) and (2) regarding the literature [41].

$$\mathrm{JRC} = \frac{1}{m}\sum_{i=1}^{m}\mathrm{JRC}_i = \frac{1}{m}\sum_{i=1}^{m}\left(32.2 + 32.47\log_{10} Z_{2i}\right), \quad (1)$$

$$Z_2 = \sqrt{\frac{1}{L}\int_{x=0}^{x=L}\left(\frac{dy}{dx}\right)^2 dx}. \quad (2)$$

Afterward, JRC of the granite joint was calculated, and joint specimens with JRC = 4 were selected for the shear-flow coupling test.

Although we prepared a large number of granite joint specimens by splitting, enough specimens could not be produced with the same roughness. Accordingly, the joint specimen with JRC = 4 was selected as the template from the split specimens, and the real 3D joints of granite were replicated using UHPC (ultra-high-performance concrete) material.

Subsequently, these replicated UHPC specimens were used to carry out the test group II in Table 1 to explore the influence of seepage pressure on the shear-flow coupling characteristics of joints. The basic physical and mechanical parameters of the granite [42] and UHPC samples were tested: density ρ, uniaxial compressive strength σ_c, tensile strength σ_t, basic friction angle φ_b, elastic modulus E, and Poisson's ratio υ. The values of each parameter are listed in Table 2. It was found that the physical and mechanical properties of the two materials were relatively consistent. Therefore, UHPC could be used to simulate the granite material for the test that followed.

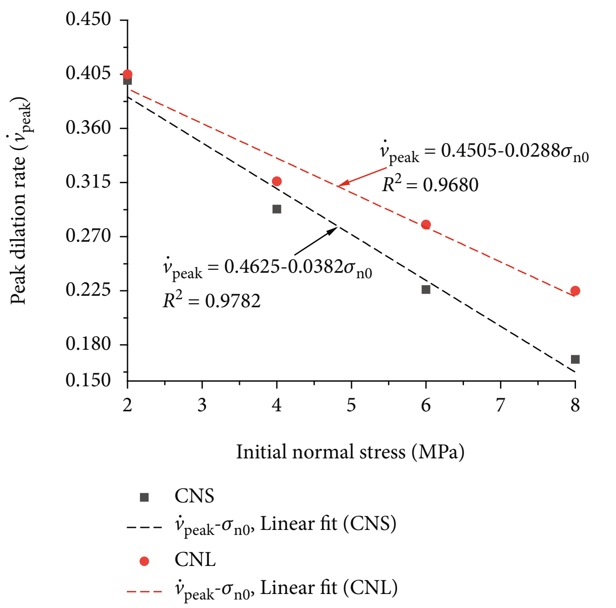

FIGURE 10: Relationship between the peak dilation rate and initial normal stress.

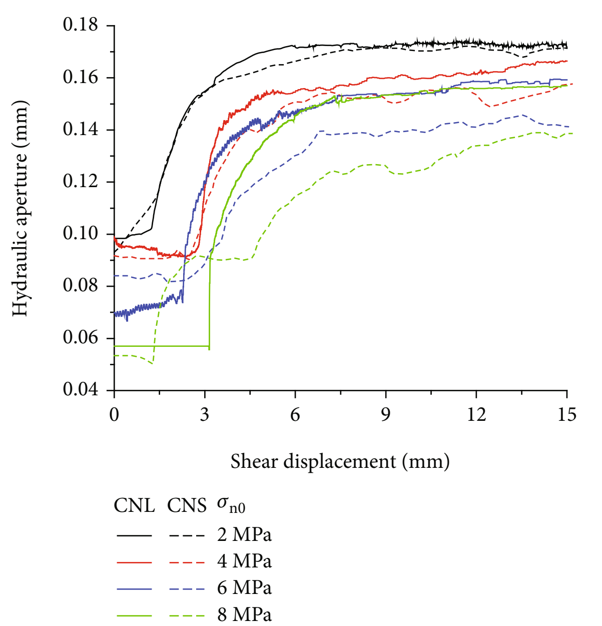

FIGURE 11: Curves of hydraulic aperture with shear displacement.

The servo-controlled rock joint shear-flow coupling test system shown in Figure 2 was utilized to perform joint shear-flow coupling tests under CNL and CNS boundary conditions.

The test was composed of the following steps.

(1) In specimen placement, the sample was placed in the shear-flow box according to the marked shear direction, and sealant was applied on the corresponding part of the inside of the shear box. (2) In the application of normal stress and lateral pressure, the normal load was applied to the set value at a rate of 0.1 kN/s, followed by the application of oil pressure greater than the seepage pressure to the lateral window of the shear-flow box. (3) In the installation of monitoring equipment, fiber-optic displacement sensors were utilized to monitor the normal displacement and shear displacement generated by the joint during the shear process. (4) In exerting seepage pressure, seepage pressure was applied to the test target value at a loading rate of 0.05 MPa/s. (5) In shear loading, the joints were sheared at a rate of 0.5 mm/min and terminated when the shear displacement reached 15 mm.

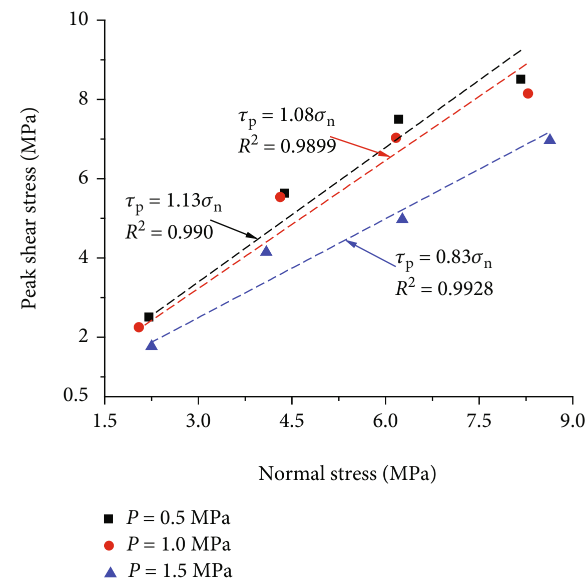

FIGURE 12: Variation of peak shear stress with normal stress.

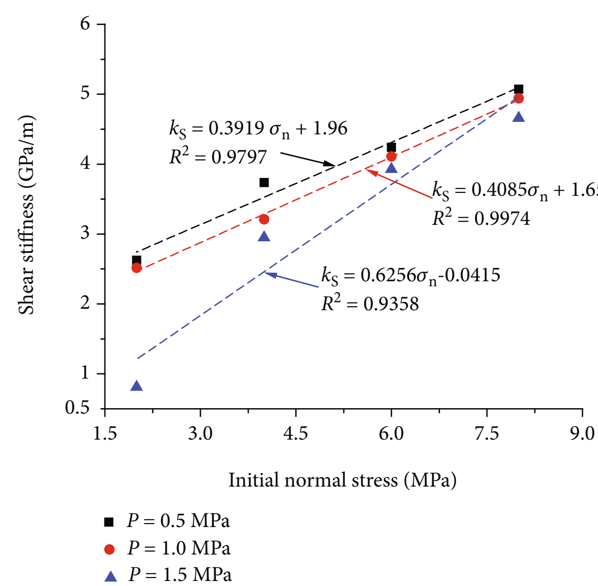

FIGURE 13: Variation of shear stiffness with initial normal stress.

3. Results and Analysis

3.1. Influence of Mechanical Boundary Conditions on Shear-Flow Coupling Characteristics of Joints

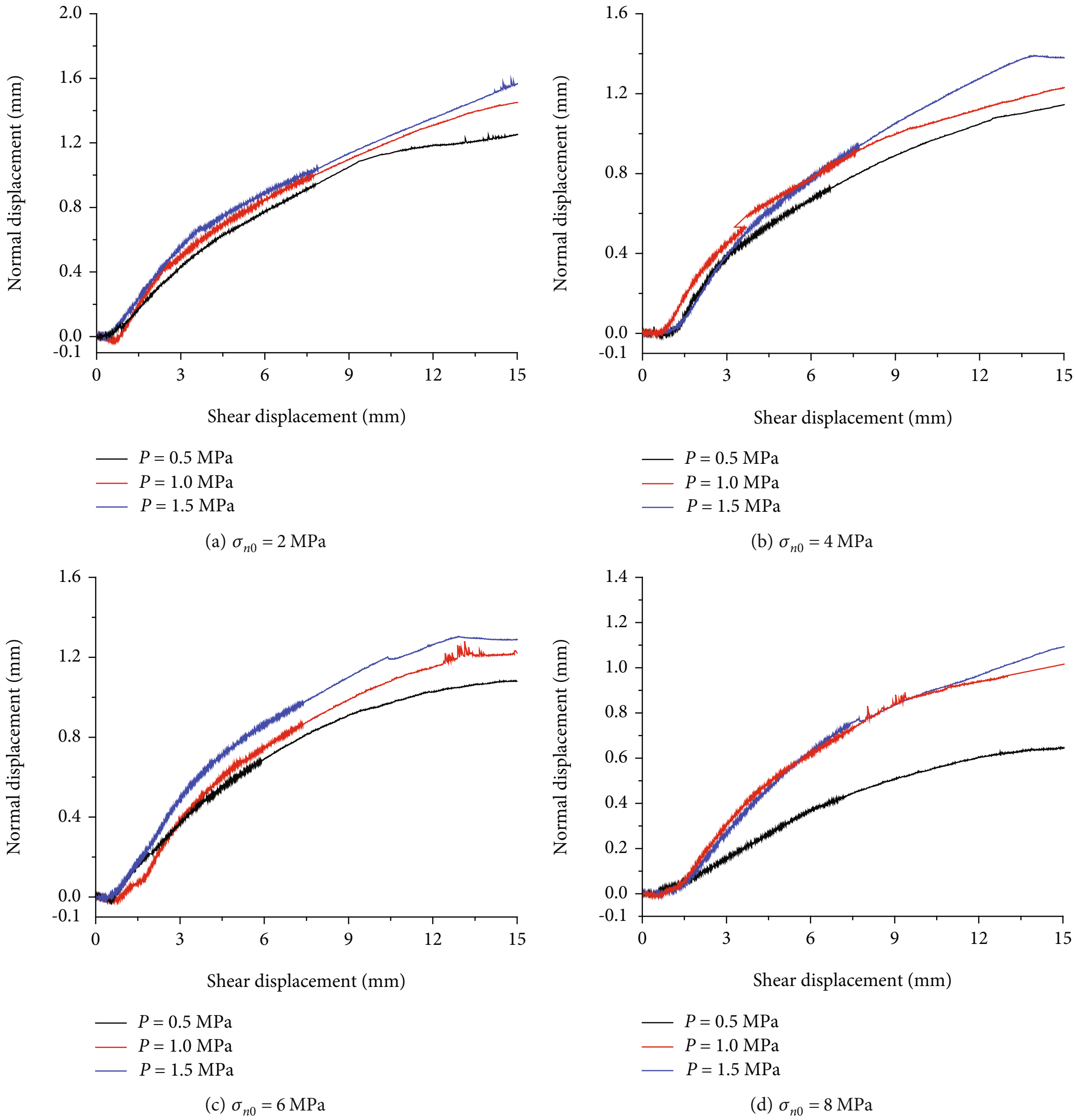

Figure 14: Curves of normal displacement with shear displacement.

3.1.1. Analysis of Shear Mechanical Characteristics of Joints. Figure 3 displays the variation curves of shear stress τ with shear displacement δ_h for the joints, both under the CNL and CNS boundary conditions. It can be observed from the figure that the shear stress increased rapidly with the shear displacement to the peak shear stress and then dropped to the residual shear stress. When the initial normal stress σ_{n0} was 2 MPa, the residual shear stress under both boundary conditions approached the peak value. Interestingly, the postpeak shear stress of the CNS boundary condition displayed a sharp decrease when $\sigma_{n0} > 2$ MPa, while the postpeak shear curves of the CNL boundary condition changed from a slowly decreasing type ($\sigma_{n0} = 4$ MPa and 6 MPa) to a sharply decreasing type ($\sigma_{n0} = 8$ MPa). In addition, the peak and residual shear stresses under both boundary conditions increased with increasing in the initial normal stress. As σ_{n0} increased from 2 MPa to 8 MPa, the peak shear stresses under CNS and CNL boundary conditions increased by 9.62 MPa and 10.19 MPa, respectively. In addition, the residual shear stresses increased by 4.49 MPa and 4 MPa, respectively. The normal load increased with dilation under the CNS boundary condition, which increased the shear resistance of the joint. This resulted in the peak and residual shear stresses under the CNS boundary condition being larger than those under the CNL boundary condition. Notably, the impact of the boundary condition on the residual shear stress was more obvious.

The slope of the prepeak linear stage of $\tau - \delta_h$ is defined as the shear stiffness k_s of the joint. It can be seen from the relationship of $k_s - \sigma_{n0}$ (Figure 4) that when σ_{n0} increased

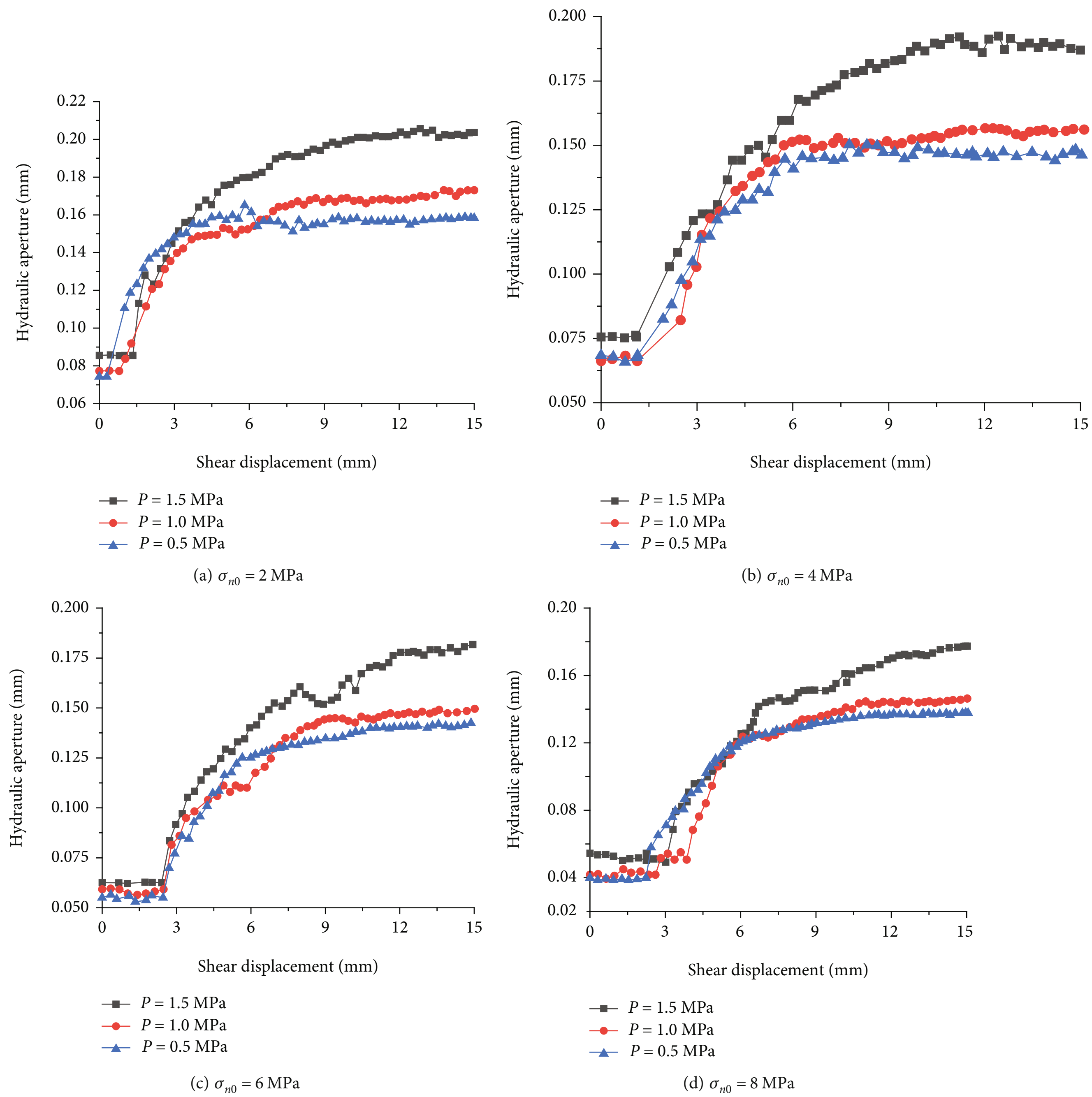

Figure 15: Curves of hydraulic aperture with shear displacement.

from 2 MPa to 8 MPa, the shear stiffness under CNS and CNL conditions increased by 2.58 GPa/m and 3.71 GPa/m, respectively. It was found that the shear stiffness of joints under the CNS boundary condition was always greater than that under CNL. After the peak shear displacement, $\tau - \delta_h$ curves exhibited a strain-softening phenomenon. As defined in Equation (3), the shear stress drop coefficient S_c represented the development of shear stress after peak shear displacement:

$$S_c = \frac{(\tau_p - \tau_r)}{\tau_p}, \tag{3}$$

where τ_p is the peak shear stress and τ_r is the residual shear stress. When $S_c = 0$ and 1, the joint exhibited ideal plasticity and ideal brittle shear behavior, respectively. The strain-softening behavior of the joint was characterized by S_c between 0 and 1.

The variation in the drop coefficient with the initial normal stress under the two boundary conditions is shown in Figure 5. In general, the softening coefficient increased with an increase in the initial normal stress. As σ_{n0} increased from 2 to 8 MPa, S_c under the CNS and CNL conditions increased by 0.527 and 0.226, respectively. In addition, it was found that S_c for the CNS boundary condition was

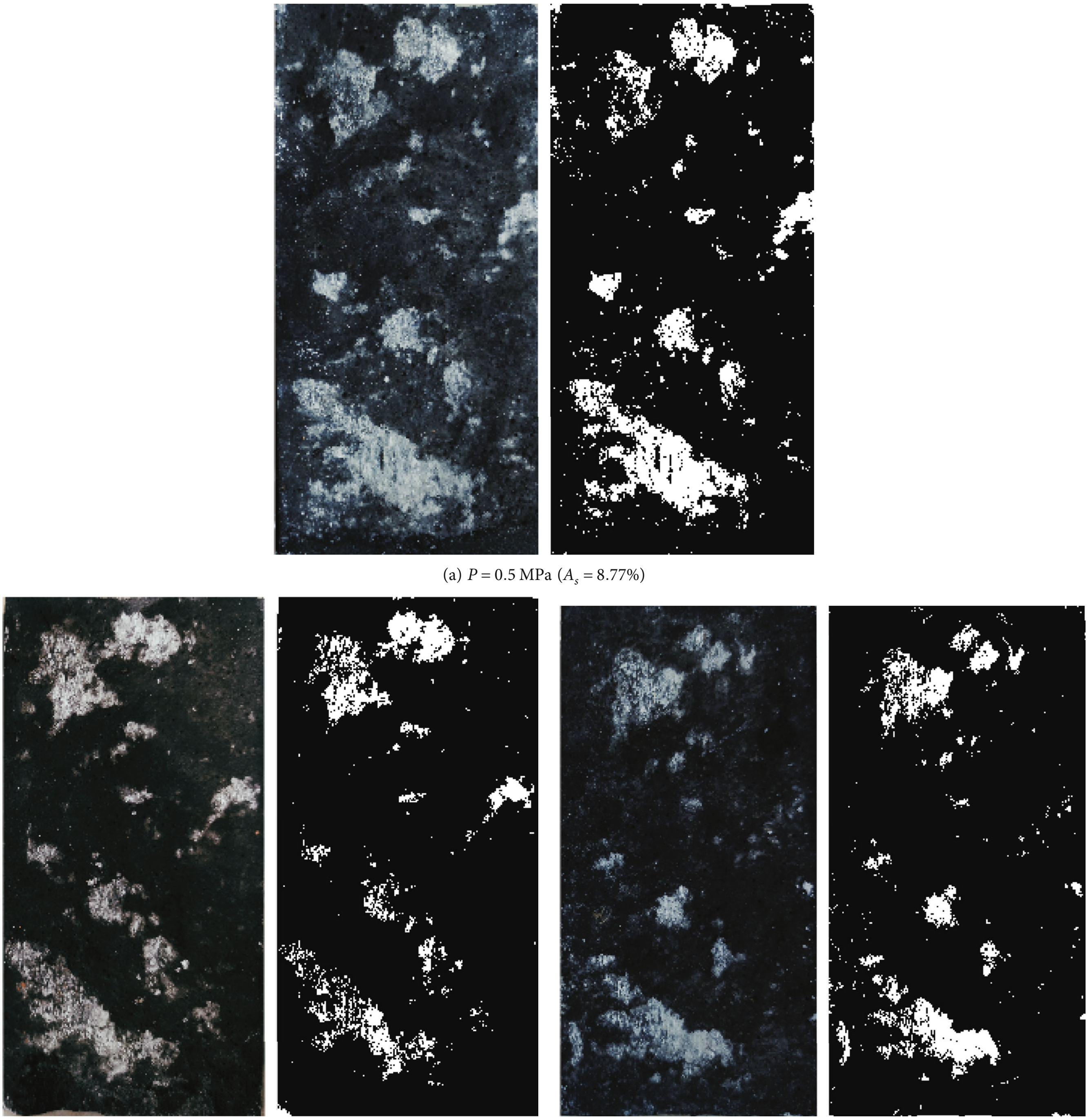

(a) $P = 0.5$ MPa ($A_s = 8.77\%$)

(b) $P = 1.0$ MPa ($A_s = 7.79\%$)

(c) $P = 1.5$ MPa ($A_s = 6.22\%$)

Figure 16: Failure condition of the joint when the initial normal stress is 2 MPa.

always smaller than that for the CNL condition, indicating that the strain-softening phenomenon was more significant in the CNL boundary condition as compared to CNS.

Based on the evolution curves of shear stress path with normal stress under CNS boundary conditions (Figure 6), normal stress continuously increased with shear displacement. At the same time, the shear stress showed the phenomenon of "increase rapidly-drop-stability" ($\sigma_{n0} > 2$ MPa) or "increase rapidly-increase slowly" ($\sigma_{n0} = 2$ MPa) with normal stress. By linear fitting of τ_p and τ_r with normal stress, the shear peak and residual friction angle under CNS boundary conditions were 53.7° and 35.3°, respectively, and the friction angle was reduced by 34.3%. Similarly, the relationships of $\tau_p - \sigma_{n0}$ and $\tau_r - \sigma_{n0}$ under CNL boundary conditions were linearly fitted (Figure 7), and the peak and residual friction angle were 52° and 33.4°, respectively. This indicated that both the peak and residual friction angles for the CNL boundary condition were lower than those for CNS condition.

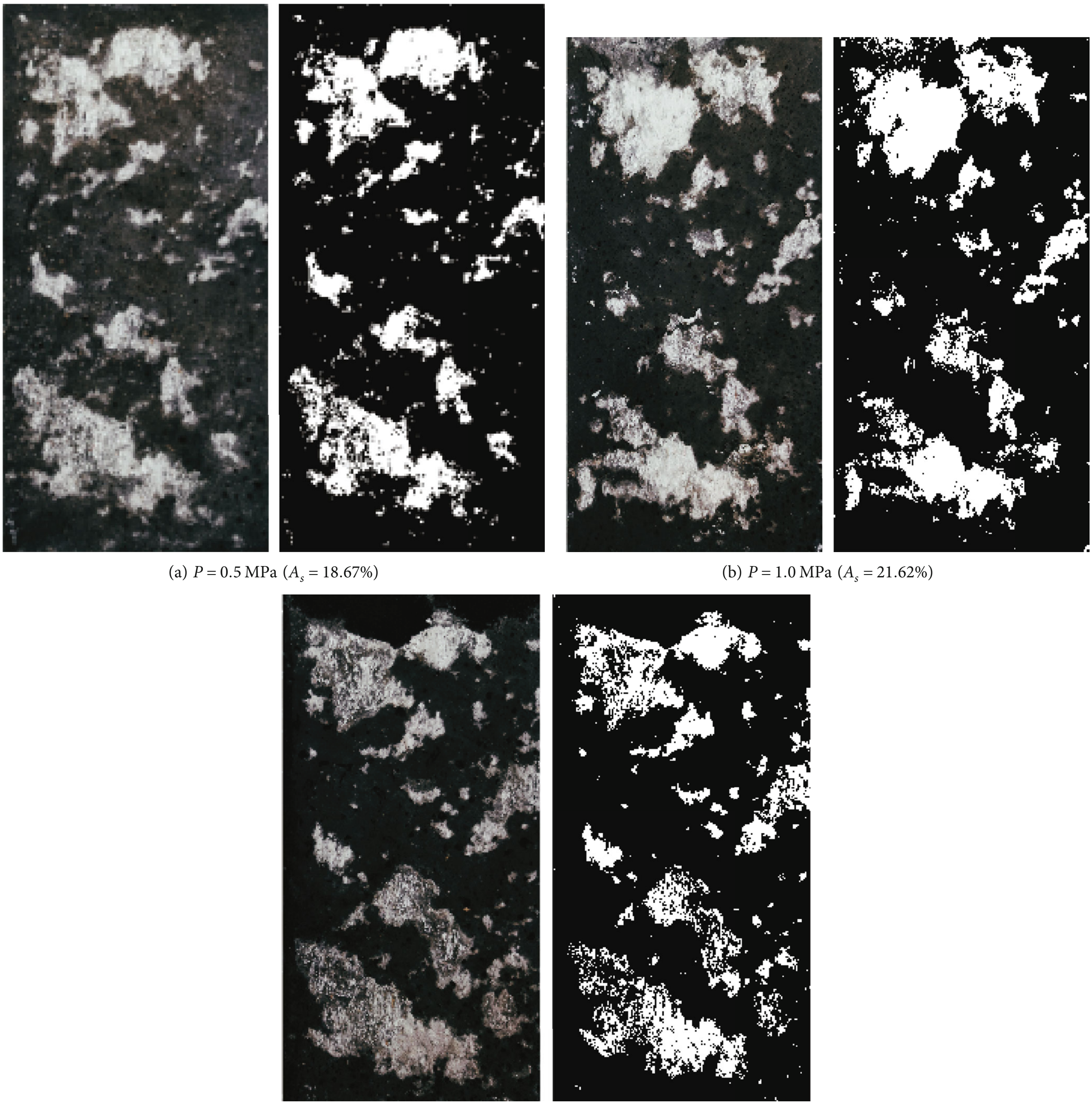

(a) $P = 0.5$ MPa ($A_s = 18.67\%$)

(b) $P = 1.0$ MPa ($A_s = 21.62\%$)

(c) $P = 1.5$ MPa ($A_s = 17.35\%$)

FIGURE 17: Failure condition of the joint when the initial normal stress is 8 MPa.

3.1.2. Analysis of Influence on Joint Dilation Characteristics. Figure 8 displays the relationship between normal and shear displacements under CNS and CNL boundary conditions. The joints gradually closed under normal stress during the initial shear phase for both boundary conditions, resulting in shear shrinkage. Subsequently, the joint exhibited dilation behavior as the shear displacement continued to increase. The smaller the initial normal stress, the more obvious the dilation phenomenon. With the continuous development of the shear displacement, the dilation effect gradually weakened, and the dilation curves turned flat. Furthermore, it was clearly observed throughout the shearing process that the normal displacements for the CNS condition were always smaller than those for CNL, and this difference became apparent as the initial normal stress increased. Taking δ_{v-15} as an example (δ_{v-15} was the normal displacement when $\delta_h = 15$ mm), the difference of δ_{v-15} under the two boundary conditions increased from

0.03 mm to 0.18 mm as the initial normal stress increased from 2 MPa to 8 MPa.

Parameter λ was defined as the ratio of shear displacement δ_h to peak shear displacement $\delta_{h-\text{peak}}$, that is, $\lambda = \delta_h/\delta_{h-\text{peak}}$. In addition, the dilation rate $\dot{v}$, was obtained by the first-order differential of the normal displacement-shear displacement curve (Figure 9). The dilation rate showed three stages of "increase rapidly-drop-stability." First, when λ increased from a negative value to 0, it corresponded to the joint shear shrinkage stage. Subsequently, the joint entered the dilation stage with a rapid increase in λ and reached a maximum value when λ increased to 1, which was the peak dilation rate $\dot{v}_{\text{peak}}$. When $\lambda > 1$, the dilation rate decreased continuously until it approached 0, and the dilation effect gradually disappeared at this stage.

The peak dilation rate for the two boundary conditions was well fitted linearly to the initial normal stress (Figure 10). The initial normal stress increased from 2 MPa to 8 MPa, as the $\dot{v}_{\text{peak}}$ under CNS and CNL boundary conditions decreased by 57.5% and 44.4%, respectively. Notably, under the CNS boundary condition, the normal stress continues to increase with the increase of shear displacement, thereby inhibiting the dilation effect of joints, resulting in that the peak dilation rate under the CNS condition is always lower than that under the CNL condition.

3.1.3. Analysis of the Influence on Hydraulic Aperture. The cubic law is an approximate description of the seepage law of joints with smooth and straight walls on both sides, large opening and no filling [43]. The cubic law shown in Equation (4) was used to calculate the hydraulic aperture of the joint during shear-flow coupling test:

$$Q = -\frac{we^3}{12\mu}\nabla P, \tag{4}$$

where Q is the flow rate (m^3/s), e is the joint hydraulic aperture (m), μ is the dynamic viscosity coefficient (Pa·s), and ∇P is the macroscopic pressure gradient along the flow direction, which is equal to the pressure drop between the inlet and outlet divided by the joint length.

Based on the variation curves of hydraulic aperture with shear displacement under different initial normal stresses (Figure 11), the hydraulic aperture under the two boundary conditions showed a four-stage variation law of "steady-sudden increase-slow increase-basically stable."

In the initial shear stage, the hydraulic aperture under the CNS and CNL boundary conditions displayed a stable phenomenon with an increase in shear displacement owing to the insignificant dilation effect of the joints. Subsequently, the normal displacement increased rapidly, and the hydraulic aperture entered the stage of "sudden increase" at approximately the peak shear displacement. The joint dilation effect began to diminish with the development of the shear displacement; that is, the aperture displayed a phenomenon of "slow increase."

The joint dilation effect gradually disappeared when the shear displacement developed to a certain extent. Thus, the hydraulic aperture shows a state of "basically stable." Furthermore, it can be clearly observed from the figure that the hydraulic aperture under the two boundary conditions decreased with increase in the initial normal stress, and the hydraulic aperture under the CNS condition was always lower than that under CNL. The greater the initial normal stress, the stronger the influence of the normal stiffness boundary condition on the hydraulic aperture e_{15} (e_{15} was the hydraulic aperture when $\delta_h = 15$ mm). With the initial normal stress increasing from 2 MPa to 8 MPa, the difference in e_{15} increased from 0.001 mm to 0.180 mm under the two boundary conditions. It should be noted that under CNL boundary conditions, the curve appears abnormal when $\sigma_{n0} = 8$ MPa. For this abnormal phenomenon, we believe that although the hydraulic aperture is closely related to the normal displacement in the shear-flow coupling process, the granite joints with the same JRC prepared by splitting cannot guarantee the complete consistency of their morphology. As a result, the seepage channel is blocked to varying degrees in the shear process, so the hydraulic aperture calculated by the cubic law is abnormal.

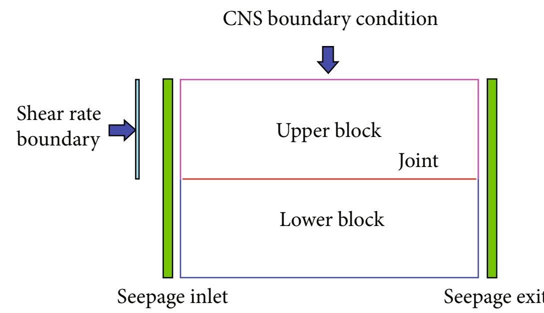

Figure 18: Shear-flow coupling numerical experimental model.

3.2. Influence of Seepage Pressure Boundary Conditions on Joint Shear-Flow Coupling Characteristics

3.2.1. Analysis of Influence on Shear Mechanical Characteristics. Figure 12 shows the relationship between peak shear stress and normal stress under three level seepage pressure, which was 0 MPa, 1 MPa, and 1.5 MPa, respectively. The average peak shear stress decreased from 6.0 MPa to 4.5 MPa when the seepage pressure increased from 0.5 MPa to 1.5 MPa, which was a reduction of 25%. Meanwhile, the peak shear stress decreased most obviously when $P = 1.5$ MPa. Therefore, it can be considered that the weakening effect of seepage pressure on shear strength will be strengthened with an increase in seepage pressure. As shown in Figure 13, it displayed a decreasing trend for the peak friction angle of the joint owing to the increase in seepage pressure. The peak friction angle decreased from 48.5° to 39.7° with the increase of seepage pressure from 0.5 MPa to 1.5 MPa, which was a reduction of 18.1%. This phenomenon also explained, to some extent, the increase in seepage pressure leading to a decrease in the friction angle which affected the peak shear strength of the joint.

Based on the relationship between joint shear stiffness and the initial normal stress under different seepage pressures (Figure 13), joint shear stiffness decreased with the

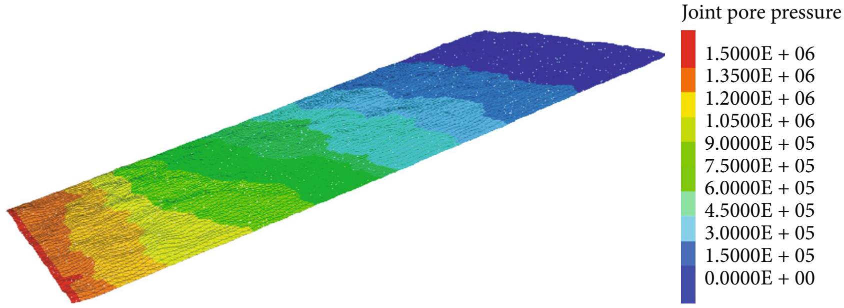

Figure 19: Numerical model of single joint and cloud diagram of seepage pressure distribution.

Table 3: Parameters of M-C model.

P (kg·m^{-3})	E (GPa)	ν	σ_t (MPa)	C (MPa)	φ (°)
2320	14.7	0.21	9.1	26.84	51

Table 4: Mechanical parameters of C-Y model.

k_s (GPa·m^{-1})	k_n (GPa·m^{-1})	e_n	e_s	R (mm)	$\varphi(i)m$ (°)	φ_b (°)	a_{zero} (m)	$a_{\max}$ (m)	a_{res} (m)
3.93	14.63	1	1	3.6	39.7	30.4	6×10^{-5}	1.28×10^{-3}	1×10^{-6}

increase in seepage pressure. This was because the seepage pressure reduced the effective normal stress of the joint surface and the lubrication effect of seepage on the joint surface. The average shear stiffness under four-stage initial normal stress decreased from 3.92 GPa/m to 3.09 GPa/m with the increase of seepage pressure from 0.5 MPa to 1.5 MPa. Notably, the shear stiffness decreased most significantly under the condition of $\sigma_{n0} = 2$ MPa and $P = 1.5$ MPa.

3.2.2. Analysis of Influence on Joint Dilation Characteristics. Based on the relationship between normal displacement and shear displacement under different seepage pressures (Figure 14), normal displacement under the three level seepage pressures showed a consistent feature. That is, the normal displacement decreased, owing to the shear shrinkage behavior of joints in the early stage of shear, but the decrease was small; subsequently, the normal displacement increased slowly, with gradual weakening of the amplitude. In Figure 14, the normal displacement curve was rough and fluctuant. We analyzes that during the shearing process, joint asperities will be sheared off and damaged to form the fragments. During the staggered movement of the joint, the dilation of the fragments will lead to a small increase in the normal displacement, and the fragment will be easily crushed and destroyed or transported to cause a small decrease in the normal displacement. At the same time, the role of seepage pressure intensifies the transfer of fragments.

In addition, the dilation effect of the joint also increased with increasing seepage pressure, which is the same as that of Yin and Chen [37]. Incorporating the normal displacement when the shear displacement was 15 mm as an example, the average normal displacement under the four-stage initial normal stress increased from 1.03 mm to 1.78 mm with an increase in the seepage pressure from 0.5 MPa to 1.5 MPa.

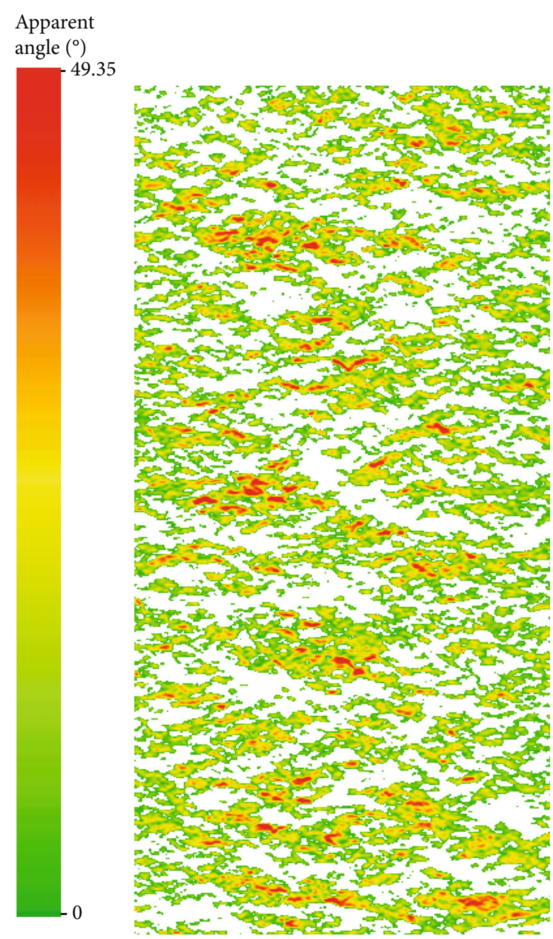

Figure 20: Distribution of apparent dip angle of joint asperities.

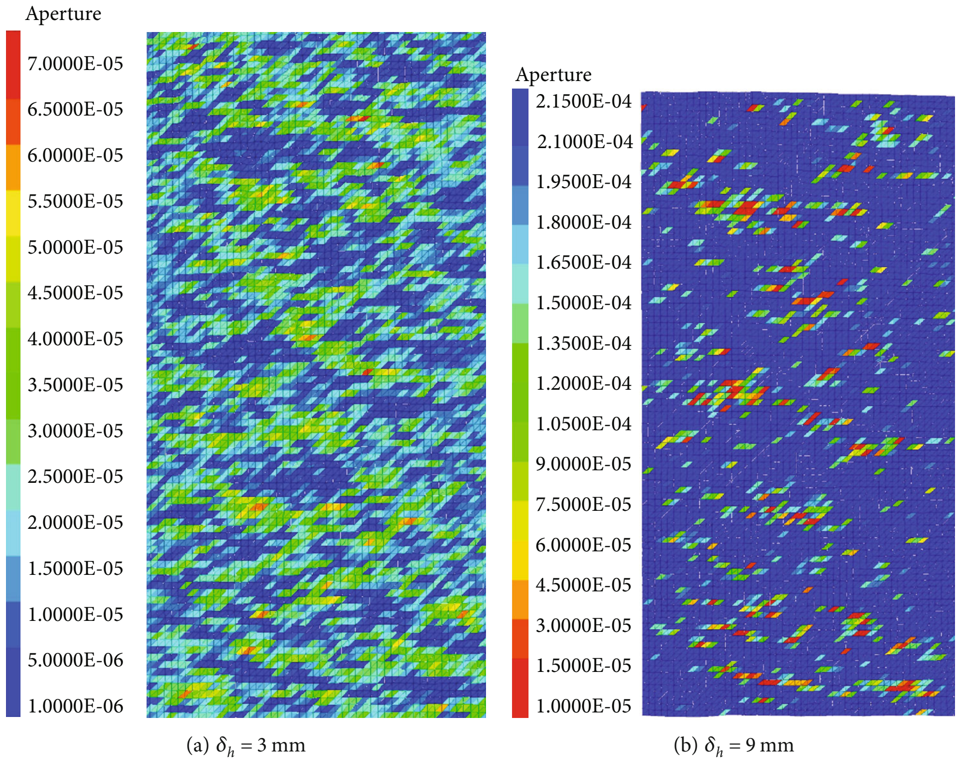

FIGURE 21: Evolution of hydraulic aperture during shearing.

3.2.3. Analysis of Influence on Hydraulic Aperture. Figure 15 displays the variation curves of the hydraulic aperture with shear displacement under different seepage pressures. Overall, the hydraulic aperture under different seepage pressures shows relatively consistent characteristics, that is, it showed four changing rules of "steady-sudden increase-slow increase-basically stable."

It can be clearly observed from Figure 15 that the joint hydraulic aperture increased with an increase in seepage pressure. Taking the hydraulic aperture e_{h-15} at shear displacement of 15 mm as the stable hydraulic aperture, the average value (under initial normal stress at four levels) of e_{h-15} increased from 0.146 mm to 0.187 mm with an increase in the seepage pressure from 0.5 MPa to 1.5 MPa. This was because the seepage pressure enhanced the dilation effect of the joint surface.

3.3. Variation Law of Joint Morphology under Shear-Flow Coupling. MATLAB programming was used to binarize the joint surface image after shearing, to study the failure characteristics of the joint surface under shear–flow coupling. The shear failure zone was defined as white and the rest as black. The ratio of the shear area to the total area of the joints was defined as the shear area ratio A_s, which represented the degree of joint failure. Figures 16 and 17 display the failure and binary images of the joint surfaces when the initial normal stresses are 2 MPa and 8 MPa, respectively, under different seepage pressures. It should be noted that the failure condition refers to the final failure state when the shear displacement reaches 15 mm.

Based on the wear morphology characteristics of the joint surface post shear, it can be observed that the zones of wear-out failure occur at the high asperities of the joint surface. Therefore, it can be considered that high asperities play a key role in the shear process. The binary images also indicate that the failure degree of the joint surface increased with an increase in the initial normal stress. The average A_s (under different water pressures) of joint surface increased from 7.59% to 19.21% when initial normal stress increased from 2 MPa to 8 MPa. In addition, seepage pressure affected the wear area of the joint surface to a certain extent. Taking the wear of joint surface ($\sigma_{n0} = 2$ MPa) as an example, the seepage pressure increased from 0.5 MPa to 1.5 MPa, and the proportion of wear area decreases from 8.77% to 6.22%. In other words, the wear area demonstrates a decreasing trend with an increase in seepage pressure. Interestingly, this characteristic was not obvious when $\sigma_{n0} = 8$ MPa. In fact, this rule was not controlled by seepage pressure alone, but the result of two factors: seepage pressure reduced the effective normal stress; nevertheless, the applied normal stiffness increased the normal stress owing to joint dilation. It is worth noting that the factors affecting the joint morphology are not limited to normal stress and seepage pressure, but also influenced by gouge resulting from the shear-flow process. However, other influencing factors could not be directly reflected in this test, so only the influence of normal stress and osmotic water pressure on the joint surface morphology was analyzed.

3.4. Numerical Experimental Study on Seepage Path Evolution in Joint Shear Process

3.4.1. Introduction to Numerical Simulation. Based on the 3DEC simulation software, a rough three-dimensional

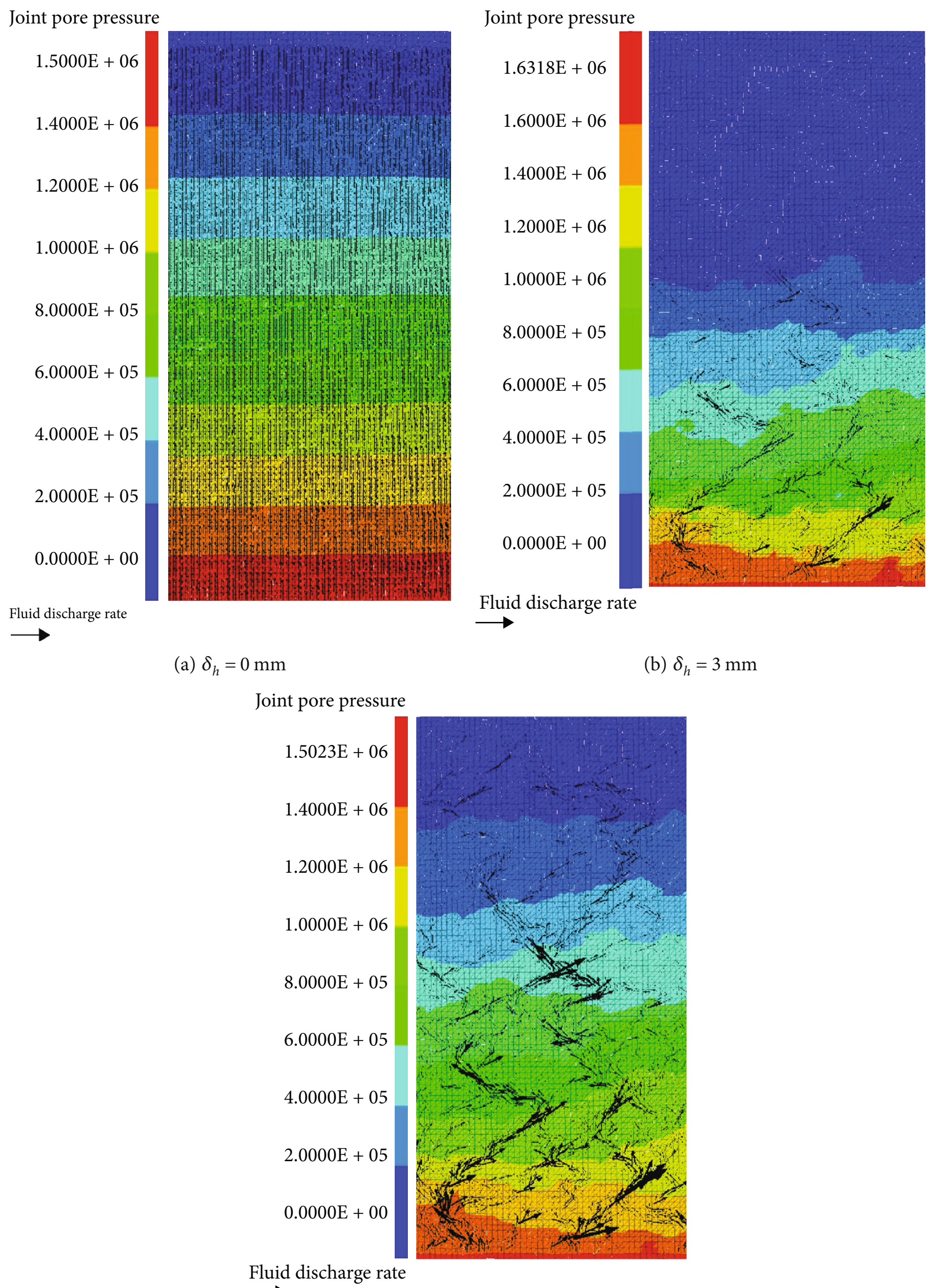

(a) $\delta_h = 0$ mm

(b) $\delta_h = 3$ mm

(c) $\delta_h = 9$ mm

FIGURE 22: Evolution law of seepage pressure and seepage path.

single joint model with JRC = 4 was constructed. Typical hydromechanic conditions ($\sigma_{n0} = 6$ MPa, $P = 1.5$ MPa) were set to carry out the shear-flow coupling numerical experiment under CNS boundary conditions to visually reflect the seepage path and hydraulic aperture distribution of the joint in the shear process, which could complement the laboratory tests.

The size of the numerical model was consistent with that of the sample used in the laboratory test, consisting of upper and lower blocks and a joint plane. The size of the two rock blocks was $200 \times 100 \times 50$ mm, and the joint length was 200 mm. The numerical model is shown in Figure 18. The CNS boundary condition was applied to the upper surface of the model. The left side of the upper block was a constant shear rate boundary with a rate of 0.001 mm/min, and the lower block remained fixed. Seepage pressure was applied on the left side of the model, and the right side was considered as the zero-water pressure boundary. Figure 19 displays the joint geometric model and cloud diagram of seepage pressure distribution.

In this numerical experiment, the M-C constitutive model was used for the blocks, and the continuous yield joint model (C-Y model) was selected for the joint. The model parameters were determined based on laboratory tests. The parameters required for the block constitutive model were density ρ, elastic modulus E, Poisson's ratio ν, tensile strength σ_t, cohesion c, and internal friction angle φ. The values of each parameter are listed in Table 3. The mechanical parameters in the C-Y model included shear stiffness k_s, normal stiffness k_n, normal stiffness index e_n, shear stiffness index e_s, roughness parameter R, initial friction angle $\varphi(i)m$, basic friction angle φ_b, initial hydraulic aperture a_{zero}, maximum hydraulic aperture $a_{\max}$, and residual hydraulic aperture a_{res}. The determination method for each parameter was as given by Gao et al. [44]. They can be determined by referring to the test results of the variation range of equivalent hydraulic aperture under the condition of constant normal stiffness and normal stress of 6 MPa in Figure 15, and the values of each parameter are listed in Table 4. The hydraulic parameters which included the bulk modulus of water, density of water, and the viscosity coefficient of water were 2×10^9 Pa, 1000 kg m^{-3}, and 1×10^{-3} Pa s, respectively.

3.5. Analysis of Numerical Experimental Results. For an improved description of the seepage law on the joint surface, we demonstrate the distribution of the apparent dip angle of the joint asperities (Figure 20). The distribution of the hydraulic aperture during the shear process is demonstrated in Figure 21. As shown in Figure 21(a), owing to the climbing and interlocking action of the joint when $\delta_h = 3$ mm, the back shear surface detached and formed several cavities, resulting in a large hydraulic aperture being distributed in the cavity position of the back shear surface. With the further development of shear displacement, the joint surface continued to dilate, and the hydraulic aperture increased accordingly. Subsequently, the shear behavior entered the residual stage, and the dilation effect weakened. By comparing Figures 20 and 21(b), it can be seen that the asperities with large undulant asperities of the joint surface play a major role in dilation in the residual stage, and most of the contact surfaces were detached to form several cavities. This resulted in a uniform distribution of the hydraulic aperture on the entire joint surface, except for a smaller hydraulic aperture at the position of steeper asperities on the shear surface (Figure 21(b)).

Figure 22 shows the evolution law of seepage pressure and seepage path of the joint surface during the shear process. It can be observed that the seepage pressure of the joint surface gradually decreased along the shear direction when $\delta_h = 0$ (Figure 22(a)). At the same time, because the initial hydraulic aperture was set, water flowed along the entire joint surface, but the flow rate was small. When the shear displacement changed to 3 mm, water flowed in the cavity regions where the contact surfaces separated from each other, and seepage channels were gradually formed (Figure 22(b)). As the shearing continued, the large dilation caused most of the asperities to separate when $\delta_h = 9$ mm (Figure 22(c)), and the water flowed almost along the entire joint surface. However, because of the joint contact with each other at undulant asperities with large sizes, seepage bypassed these contact regions. As a result, dominant seepage channels were formed, and a larger flow rate appeared at the intersection of the seepage channels.

4. Conclusions

(1) The peak and residual shear stresses under the CNS and CNL boundary conditions increased with an increase in the initial normal stress. In addition, the peak and residual shear stresses under the CNS boundary conditions were greater than those under the CNL boundary conditions. When the initial normal stress increased from 2 MPa to 8 MPa, the shear stiffness under CNS and CNL boundary conditions increased by 2.58 GPa/m and 3.71 GPa/m, respectively. The shear stiffness under the CNS boundary condition was always greater than that under CNL. In general, the larger the initial normal stress, the more obvious the drop extent of the post-peak shear stress. Compared to the CNS boundary condition, the drop phenomenon of shear stress under CNL condition was more significant.

(2) The normal displacement of the joint under the CNS boundary condition was always lower than that under CNL. The dilation rate displayed three stages of "increase rapidly-drop-stability" with the ratio of shear displacement to peak shear displacement. When the initial normal stress increased from 2 MPa to 8 MPa, the peak dilation rate under CNS and CNL boundary conditions decreased by 57.5% and 44.4%, respectively. In addition, the peak dilation rate under CNS boundary conditions was always lower than that under CNL

(3) The seepage pressure increased from 0.5 MPa to 1.5 MPa, the average peak shear stress at all levels of initial normal stress decreased from 6.0 MPa to 5.1 MPa, the peak friction angle decreased from 48° to 39.8°, and the average shear stiffness decreased from 3.92 GPa/m to 3.09 GPa/m under the four initial normal stresses. In the shear process, the hydraulic aperture increased with the increase in seepage pressure, experiencing a four-stage change rule of "steady-sudden increase-slow increase-basically stable," and the hydraulic aperture under the CNS boundary condition was always lower than that under CNL

(4) The initial normal stress increased from 2 MPa to 8 MPa, and the proportion of average wear area at all levels of seepage pressure of joints increased from 7.59% to 19.21%. The influence of seepage pressure on the wear failure of the joint surface was controlled by two factors: the seepage pressure reduced the effective normal stress; nevertheless, the applied

normal stiffness increased the normal stress owing to joint dilation

(5) The numerical experimental results demonstrated that seepage flows along the entire joint surface before joint shear. The maximum hydraulic aperture was distributed at the joint cavity regions with the development of shear displacement, and seepage channels were gradually formed. When the shear entered the residual stage, a uniform distribution of the hydraulic aperture was observed on the entire joint surface, except for a smaller hydraulic aperture at the position of steeper asperities on the shear surface. The seepage bypassed the contact regions of the fluctuant asperities with large sizes, forming obvious dominant seepage channels on the joint surface. A higher flow rate with larger magnitude appeared at the intersection of the seepage channels

Data Availability

The data used to support the findings of this study are available from the corresponding author upon request.

Conflicts of Interest

The authors declare that there is no conflict of interest regarding the publication of this paper.

Acknowledgments

This research was funded by the Opening Fund of Key Laboratory of Geohazard Prevention of Hilly Mountains, Ministry of Natural Resources (Fujian Key Laboratory of Geohazard Prevention) (Grant No. FJKLGH2022K002) and by the Geological Research Project of Bureau of Geology and Mineral Exploration and Development Guizhou Province of China (Grant No. Qiandikuang Kehe [2020] No.1).

References

[1] T. Koyama, I. Neretnieks, and L. Jing, "A numerical study on differences in using Navier-Stokes and Reynolds equations for modeling the fluid flow and particle transport in single rock fractures with shear," *International Journal of Rock Mechanics and Mining Sciences*, vol. 45, no. 7, pp. 1082–1101, 2008.

[2] S. Sisavath, A. Al-Yaarubi, C. C. Pain, and R. W. Zimmerman, "A simple model for deviations from the cubic law for a fracture undergoing dilation or closure," *Pure and Applied Geophysics*, vol. 160, no. 5-6, pp. 1009–1022, 2003.

[3] Y. Xue, J. Liu, P. G. Ranjith, F. Gao, H. Xie, and J. Wang, "Changes in microstructure and mechanical properties of low-permeability coal induced by pulsating nitrogen fatigue fracturing tests," *Rock Mechanics and Rock Engineering*, 2022.

[4] C. Wang, Y. Jiang, H. Luan, and S. Sugimoto, "Effect of shearing on hydraulic properties of rough-walled fractures under different boundary conditions," *Energy Science and Engineering*, vol. 8, no. 3, pp. 865–879, 2020.

[5] G. Rong, D. Hou, J. Yang, and C. B. Zhou, "Experimental study of flow characteristics in non-mated rock fractures considering 3D definition of fracture surfaces," *Engineering Geology*, vol. 220, pp. 152–163, 2017.

[6] H. M. Shen, Q. Zhang, Q. Li, X. Li, L. Shi, and N. Shen, "Experimental and numerical investigations of the dynamic permeability evolution of a fracture in granite during shearing under different normal stress conditions," *Rock Mechanics and Rock Engineering*, vol. 53, no. 10, pp. 4429–4447, 2020.

[7] M. P. Ahola, S. Mohanty, and A. Makurat, "Coupled mechanical shear and hydraulic flow behavior of natural rock joints," *Developments in Geotechnical Engineering*, vol. 79, pp. 393–423, 1996.

[8] H. S. Lee and T. F. Cho, "Hydraulic characteristics of rough fractures in linear flow under normal and shear load," *Rock Mechanics and Rock Engineering*, vol. 35, no. 4, pp. 299–318, 2002.

[9] T. Esaki, S. Du, Y. Mitani, and L. Jing, "Development of a shear-flow test apparatus and determination of coupled properties for a single rock joint," *International Journal of Rock Mechanics and Mining Sciences*, vol. 36, no. 5, pp. 641–650, 1999.

[10] Y. Fang, D. Elsworth, C. Y. Wang, T. Ishibashi, and J. P. Fitts, "Frictional stability-permeability relationships for fractures in shales," *Journal of Geophysical Research: Solid Earth*, vol. 122, no. 3, pp. 1760–1776, 2017.

[11] T. Yang, S. Wang, P. Wang, and Z. Zhang, "Hydraulic and mechanical coupling analysis of rough fracture network under normal stress and shear stress," *KSCE Journal of Civil Engineering*, vol. 26, no. 2, pp. 650–660, 2022.

[12] X. Xiong, B. Li, Y. Jiang, T. Koyama, and C. Zhang, "Experimental and numerical study of the geometrical and hydraulic characteristics of a single rock fracture during shear," *International Journal of Rock Mechanics and Mining Sciences*, vol. 48, no. 8, pp. 1292–1302, 2011.

[13] Z. Q. Zhou, Y. Zhao, and C. L. Wang, "Hydraulic and mechanical relationship of individual fracture in rock under compression and shearing: theoretical study," *Geofluids*, vol. 2020, no. 6, Article ID 8848116, 11 pages, 2020.

[14] N. Shen, X. C. Li, Q. Zhang, and L. Wang, "Comparison of shear-induced gas transmissivity of tensile fractures in sandstone and shale under varying effective normal stresses," *Journal of Natural Gas Science and Engineering*, vol. 95, article 104218, 2021.

[15] S. M. M. Niktabar, K. S. Rao, and A. K. Shrivastava, "Effect of rock joint roughness on its cyclic shear behavior," *Journal of Rock Mechanics and Geotechnical Engineering*, vol. 9, no. 6, pp. 1071–1084, 2017.

[16] B. Indraratna, S. Thirukumaran, E. T. Brown, and S. P. Zhu, "Modelling the shear behaviour of rock joints with asperity damage under constant normal stiffness," *Rock Mechanics and Rock Engineering*, vol. 48, no. 1, pp. 179–195, 2015.

[17] N. Huang, G. Han, R. Liu, and Y. Jiang, "Mechanical behaviour of rock samples containing multiple parallel joints during shearing," *Geotechnique Letters*, vol. 11, no. 2, pp. 133–139, 2021.

[18] Y. Liu, H. Zhao, M. Zhao, and J. Hou, "Laboratory and theoretical study for concrete-mudstone interface shear to account for asperity degradation," *Environmental Earth Sciences*, vol. 81, no. 1, article 10128, pp. 1–16, 2022.

[19] C. Guojian, Z. Chuanqing, and H. Huachao, "Experiment study on shear behavior of artificial joint under CNL and CNS boundary conditions," *Chinese Journal of Rock Mechanics and Engineering*, vol. 38, no. S2, pp. 3384–3392, 2022.

[20] B. Indraratna and A. Haque, "Experimental study of shear behavior of rock joints under constant normal stiffness conditions," *International Journal of Rock Mechanics and Mining Sciences*, vol. 34, no. 3-4, pp. 141.e1–141.e14, 1997.

[21] B. Indraratna, H. S. Welideniya, and E. T. Brown, "A shear strength model for idealised infilled joints under constant normal stiffness," *Géotechnique*, vol. 55, no. 3, pp. 215–226, 2005.

[22] Y. K. Lee, J. W. Park, and J. J. Song, "Model for the shear behavior of rock joints under CNL and CNS conditions," *International Journal of Rock Mechanics and Mining Sciences*, vol. 70, pp. 252–263, 2014.

[23] O. M. Usol'Tseva, P. A. Tsoi, and V. N. Semenov, "Experimental study of shear behavior of rock joints under two types of boundary conditions: constant normal load and constant normal stiffness," in *IOP Conference Series: Earth and Environmental Science*, vol. 459, 2020no. 4, Article ID 042019.

[24] A. K. Shrivastava and K. S. Rao, "Physical modeling of shear behavior of infilled rock joints under CNL and CNS boundary conditions," *Rock Mechanics and Rock Engineering*, vol. 51, no. 1, pp. 101–118, 2018.

[25] R. Olsson and N. Barton, "An improved model for hydromechanical coupling during shearing of rock joints," *International Journal of Rock Mechanics and Mining Sciences*, vol. 38, no. 3, pp. 317–329, 2001.

[26] S. Chiba, Y. Ohnishi, H. Ohtsu, S. Nishiyama, and T. Yano, "The development of new apparatus considering the effect of shear deformation on hydraulic characteristics of a single joint," *Environmental Rock Engineering*, pp. 93–100, 2003.

[27] B. Li, Y. Jiang, T. Koyama, L. Jing, and Y. Tanabashi, "Experimental study on hydro-mechanical behaviour of rock joints by using parallel-plates model containing contact area and artificial fractures," *International Journal of Rock Mechanics and Mining Sciences*, vol. 45, no. 3, pp. 362–375, 2008.

[28] Q. Yin, G. W. Ma, H. W. Jing et al., "Hydraulic properties of 3D rough-walled fractures during shearing: an experimental study," *Journal of Hydrology*, vol. 555, pp. 169–184, 2017.

[29] W. B. Sun, Y. Xue, L. Yin, and J. Zhang, "Experimental study on seepage characteristics of large size rock specimens under three-dimensional stress," *Geomechanics and Engineering*, vol. 18, no. 6, pp. 567–574, 2019.

[30] M. Javadi, M. Sharifzadeh, K. Shahriar, and Y. Mitani, "Critical Reynolds number for nonlinear flow through rough-walled fractures: the role of shear processes," *Water Resources Research*, vol. 50, no. 2, pp. 1789–1804, 2014.

[31] C. Wang, Y. Jiang, R. Liu, C. Wang, and S. Sugimoto, "Experimental study of the nonlinear flow characteristics of fluid in 3D rough-walled fractures during shear process," *Rock Mechanics and Rock Engineering*, vol. 53, no. 6, pp. 2581–2604, 2020.

[32] C. Cao, Z. G. Xua, J. R. Chai, and Y. Q. Li, "Radial fluid flow regime in a single fracture under high hydraulic pressure during shear process," *Journal of Hydrology*, vol. 579, pp. 124142–124142, 2019.

[33] G. Rong, J. Yang, L. Cheng, and C. B. Zhou, "Laboratory investigation of nonlinear flow characteristics in rough fractures during shear process," *Journal of Hydrology*, vol. 541, pp. 1385–1394, 2016.

[34] S. T. Di, C. Jia, W. G. Qiao, W. J. Yu, and K. Li, "Theoretical and experimental investigation of characteristics of single fracture stress-seepage coupling considering microroughness," *Mathematical Problems in Engineering*, vol. 2017, no. 7, Article ID 6431690, 12 pages, 2017.

[35] X. Zhang, J. Chai, Y. Qin, J. Cao, and C. Cao, "Experimental study on seepage and stress of single-fracture radiation flow," *KSCE Journal of Civil Engineering*, vol. 23, no. 3, pp. 1132–1140, 2019.

[36] A. Q. Wu, L. Fan, X. Fu, Y. Zhang, Z. Zhong, and M. Yu, "Design and application of hydro-mechanical coupling test system for simulating rock masses in high dam reservoir operations," *International Journal of Rock Mechanics and Mining Sciences*, vol. 140, article 104638, 2021.

[37] L. M. Yin and J. T. Chen, "Experimental study of influence of seepage pressure on joint stress-seepage coupling characteristics," *Rock and Soil Mechanics*, vol. 34, no. 9, pp. 2563–2568, 2013.

[38] C. C. Xia, Q. F. Yu, X. Qian, Y. Gui, and X. Q. Zhuang, "Experimental study of shear-seepage behaviour of rock joints under constant normal stiffness," *Rock and Soil Mechanics*, vol. 41, no. 1, pp. 57–66+77, 2020.

[39] Y. B. Cao, X. T. Feng, E. C. Yan et al., "Calculation method and distribution characteristics of fracture hydraulic aperture from field experiments in fractured granite area," *Rock Mechanics and Rock Engineering*, vol. 49, no. 5, pp. 1629–1647, 2016.

[40] Y. Jiang, J. Xiao, Y. Tanabashi, and T. Mizokami, "Development of an automated servo-controlled direct shear apparatus applying a constant normal stiffness condition," *International Journal of Rock Mechanics and Mining Sciences*, vol. 41, no. 2, pp. 275–286, 2004.

[41] R. Tse and D. M. Cruden, "Estimating joint roughness coefficients," *International Journal of Rock Mechanics and Mining Sciences and Geomechanics Abstracts*, vol. 16, no. 5, pp. 303–307, 1979.

[42] Y. Y. Zhang, Y. B. Cao, Z. J. Li, Y. Chen, and Z. Huang, "Mechanical properties and failure mechanism of granite with maximum free water absorption under triaxial compression," *Applied Sciences*, vol. 12, no. 8, pp. 3930–3946, 2022.

[43] R. W. Zimmerman and G. S. Bodvarsson, "Hydraulic conductivity of rock fractures," *Transport in porous media*, vol. 23, no. 1, pp. 1–30, 1996.

[44] Y. H. Gao, S. C. Wu, H. Wang, and S. Xiao, "Numerical simulation of joint direct shear test based on continuously yielding joint model," *Journal of Central South University (Science and Technology)*, vol. 47, no. 4, pp. 1253–1261, 2016.